

RAMALINGAM, V., VARADHAN, P., FU, H.-C., KIM, H., ZHANG, D., CHEN, S., SONG, L., MA, D., WANG, Y., ALSHAREEF, H.N. and HE, J.-H. 2019. Heteroatom-mediated interactions between ruthenium single atoms and an MXene support for efficient hydrogen evolution. *Advanced materials* [online], 31(48), article number 1903841. Available from: <https://doi.org/10.1002/adma.201903841>

Heteroatom-mediated interactions between ruthenium single atoms and an MXene support for efficient hydrogen evolution.

RAMALINGAM, V., VARADHAN, P., FU, H.-C., KIM, H., ZHANG, D., CHEN, S., SONG, L., MA, D., WANG, Y., ALSHAREEF, H.N. and HE, J.-H.

2019

This is the accepted manuscript version of the above article, which is distributed under the Wiley terms and conditions for use of self-archived versions: <https://authorservices.wiley.com/author-resources/Journal-Authors/licensing/self-archiving.html#3>. The published version of record is available from the journal website: <https://doi.org/10.1002/adma.201903841>

Heteroatom-Mediated Interactions between Ruthenium Single Atoms and an MXene Support for Efficient Hydrogen Evolution

Vinoth Ramalingam, Purushothaman Varadhan, Hui-Chun Fu, Hyunho Kim, Daliang Zhang, Shuangming Chen, Li Song, Ding Ma, Yun Wang, Husam N. Alshareef, and Jr-Hau He**

Dr. V. Ramalingam, Dr. P. Varadhan, Dr. H. C. Fu, Prof. J. H. He
*Computer, Electrical, and Mathematical Sciences and Engineering
King Abdullah University of Science and Technology (KAUST)
Thuwal, 23955-6900, Kingdom of Saudi Arabia
E-mail: jrhou.he@kaust.edu.sa*

Prof. J. H. He
*Department of Materials Science and Engineering, City University of Hong Kong, Kowloon, Hong Kong SAR
E-mail: jrhouhe@cityu.edu.hk*

Mr. H. Kim, Prof. H. N. Alshareef
*Materials Science and Engineering, Physical Science and Engineering Division
King Abdullah University of Science and Technology (KAUST)
Thuwal, 23955-6900, Kingdom of Saudi Arabia
E-mail: husam.alshareef@kaust.edu.sa*

Dr. D. Zhang
*Imaging and Characterization Core Lab
King Abdullah University of Science and Technology (KAUST)
Thuwal 23955-6900, Kingdom of Saudi Arabia*

Dr. S. Chen, Prof. L. Song
*National Synchrotron Radiation Laboratory
CAS Center for Excellence in Nanoscience University of Science and Technology of China
Hefei, Anhui, 230029 P. R. China*

Prof. D. Ma
*Beijing National Laboratory for Molecular Sciences
College of Chemistry and Molecular Engineering and College of Engineering, and BIC-ESAT
Peking University, Beijing 100871, P. R. China*

Prof. Y. Wang
*Centre for Clean Environment and Energy, School of Environment and Science
Gold Coast Campus
Griffith University, 4222, Australia*

This is the author manuscript accepted for publication and has undergone full peer review but has not been through the copyediting, typesetting, pagination and proofreading process, which may lead to differences between this version and the [Version of Record](#). Please cite this article as [doi: 10.1002/adma.201903841](#).

This article is protected by copyright. All rights reserved.

Abstract

Herein, we employed a titanium carbide ($\text{Ti}_3\text{C}_2\text{T}_x$) MXene as an efficient solid support to host a nitrogen (N) and sulfur (S) coordinated ruthenium single atom (Ru_{SA}) catalyst, which displays superior activity toward the hydrogen evolution reaction (HER). X-ray absorption fine structure spectroscopy and aberration corrected scanning transmission electron microscopy revealed the atomic dispersion of Ru on the $\text{Ti}_3\text{C}_2\text{T}_x$ MXene support and the successful coordination of Ru_{SA} with the N and S species on the $\text{Ti}_3\text{C}_2\text{T}_x$ MXene. The resultant $\text{Ru}_{SA}\text{-N-S-Ti}_3\text{C}_2\text{T}_x$ catalyst exhibits a low overpotential of 76 mV to achieve the current density of 10 mA/cm^2 . Furthermore, we show that integrating the $\text{Ru}_{SA}\text{-N-S-Ti}_3\text{C}_2\text{T}_x$ catalyst on n^+np^+ -Si photocathode enables photoelectrochemical hydrogen production with exceptionally high photocurrent density of 37.6 mA/cm^2 that is higher than the reported precious Pt and other noble metals catalysts coupled to Si photocathodes. Density functional theory calculations suggest that Ru_{SA} coordinated with N and S sites on the $\text{Ti}_3\text{C}_2\text{T}_x$ MXene support is the origin of this enhanced HER activity. This work would extend the possibility of using the MXene family as a solid support for the rational design of various single atom catalysts.

Single atom catalysts (SACs) have emerged as a promising candidate in the field of heterogeneous catalysis.^[1] Unlike metal nanoparticles or bulk metal catalysts, SACs are atomically dispersed and isolated metal active sites that are coordinatively unsaturated. Furthermore, they demonstrate the quantum confinement effect and display metal-support interactions.^[2,3] These unique characteristics have made SACs an ideal catalyst for CO oxidation, the oxygen reduction reaction, the oxygen evolution reaction (OER), the hydrogen evolution reaction (HER), various hydrogenation reactions, CO_2 reduction, and other electrochemical applications.^[1,4,5] The catalytic activity and selectivity of SACs not only depend on the nature of the single atom but also on the solid supports that are used to disperse

the metal.^[6] Therefore, it is essential to choose an appropriate support to ensure strong interactions between the isolated SACs and the substrate in order to achieve the desired catalytic activity and selectivity. Thus far, graphene nanosheets, carbon nanotubes, and other carbon materials and metal oxides have been widely used as supports for SACs.^[5-7] Unfortunately, these materials tend to be either poor electrical conductors, electrochemically inert, or hydrophobic, which hampers the practical application of SACs for water-based electrochemical reactions.^[8,9] Thus, it is crucial to identify a solid support with excellent conductivity that is also electrochemically active and hydrophilic in order to better host isolated single atoms for electrocatalytic applications.

MXenes, a new class of two dimensional (2D) transition metal carbides/nitrides, feature exceptional properties, including i) excellent electronic conductivity with efficient charge transport, ii) catalytically active basal planes with exposed metal sites, iii) hydrophilic surface functionalities ($T_x = -O, -OH,$ and $-F$ groups), and iv) a unique layered structure consisting of conductive transition metal carbides, or metal nitrides.^[10,11] These attractive properties render MXenes as superior candidates for facilitating various electrochemical applications, including supercapacitors, Li-ion or Li-sulfur batteries, and electrocatalytic OER and HER.^[10,12,13] Notably, conductive transition-metal-carbide-based MXenes can facilitate fast electron transport to electrochemically active sites to facilitate electrochemical reactions. In addition, MXenes intercalated with water molecules can enhance ion transport in liquid electrolytes.^[14] Recently, Li et al., has demonstrated the reactive metal support interactions (RMSI) between Pt nanoparticles and transition metal carbide MXenes in which Pt nanoparticles directly bonded with the metal sites of the MXene and formed a bimetallic alloy and ordered intermetallic structures for H_2O and C-H activation applications, respectively.^[15,16] Likewise, Zhang et al., has immobilized the Pt single atoms in the Mo vacancies of $Mo_2TiC_2T_x$ and further stabilized the Pt single atoms via the formation of Pt-C

covalent bond with the surrounding carbon atoms from $\text{Mo}_2\text{TiC}_2\text{T}_x$ MXene.^[17] However, the coordination interaction between metal single atoms and MXene remains unexplored. Therefore, it is important to understand the strong coordination interactions between single atoms and MXene support via heteroatom sites and the corresponding catalytic activity.

Herein, we report the coordination interaction between isolated ruthenium single atoms (Ru_{SA}) and a 2D titanium carbide ($\text{Ti}_3\text{C}_2\text{T}_x$) MXene support through the nitrogen (N) and sulfur (S) heteroatom dopants. The Ru_{SA} are stabilized on the MXene support via the formation of Ru-N and Ru-S bonds with the N and S atoms. The Ru_{SA} -coordinated N and S species in Ru_{SA} -N-S- $\text{Ti}_3\text{C}_2\text{T}_x$ remarkably enhances the catalytic activity for HER in acidic solution. Interestingly, integrating this Ru_{SA} -N-S- $\text{Ti}_3\text{C}_2\text{T}_x$ catalyst with a n^+np^+ -Si photocathode results in an exceptionally high photocurrent density of 37.6 mA/cm^2 upon AM 1.5G illumination, outperforming the photocurrent density value of most precious noble metal integrated Si-based photocathodes reported elsewhere. Density functional theory (DFT) calculations reveal that the coordination interaction of Ru_{SA} alters the electronic structure of the $\text{Ti}_3\text{C}_2\text{T}_x$ MXene support to achieve an optimal Gibbs hydrogen adsorption free energy (ΔG_{H^*}) of close to zero, which is favorable for enhanced HER performance. We believe the findings of this study can be applied to other members of the MXene family for the rational design of highly efficient catalysts at the atomic or molecular levels.

A schematic representing the synthesis of the Ru_{SA} -N-S- $\text{Ti}_3\text{C}_2\text{T}_x$ catalyst is depicted in **Figure 1a** (see Methods for details). The $\text{Ti}_3\text{C}_2\text{T}_x$ MXene is prepared from MAX phase (M: transition metal, A: main group element, X: C and/or N) Ti_3AlC_2 using a lithium fluoride (LiF)/hydrochloric (HCl) acid mixture to selectively remove the Al layers from the MAX phase and thereby produce few-layered $\text{Ti}_3\text{C}_2\text{T}_x$ MXene (Figure 1a). To prepare the Ru_{SA} -N-S- $\text{Ti}_3\text{C}_2\text{T}_x$ electrocatalyst, we mixed $\text{Ti}_3\text{C}_2\text{T}_x$, $\text{RuCl}_3 \cdot x\text{H}_2\text{O}$, and thiourea together and then freeze-dried this material to produce a foam. The oxygen-rich surface functional groups (O

and OH groups) on the $\text{Ti}_3\text{C}_2\text{T}_x$ sheets are expected to interact with or adsorb the Ru cations, which promotes the incorporation of Ru_{SA} onto the $\text{Ti}_3\text{C}_2\text{T}_x$ support.^[18] Moreover, the freeze-drying process not only prevents the restacking of the $\text{Ti}_3\text{C}_2\text{T}_x$ MXene sheets but also helps to achieve the homogeneous distribution of Ru metal ions on the substrate.^[18] We then annealed this foam at 500 °C under inert atmosphere, which leads to the simultaneous doping of N, S, and Ru_{SA} onto the $\text{Ti}_3\text{C}_2\text{T}_x$ sheets. Transmission electron microscopy (TEM) images of the bare $\text{Ti}_3\text{C}_2\text{T}_x$ MXene nanosheet indicates the successful removal of the Al layer from the Ti_3AlC_2 starting material (Figure 1a,b, Supporting Information). Field emission-scanning electron microscopy (FE-SEM) of the final $\text{Ru}_{SA}\text{-N-S-Ti}_3\text{C}_2\text{T}_x$ product reveals the formation of a well-defined 2D nanosheet structure (Figure 1b). Likewise, TEM images further confirm the layered structure of $\text{Ru}_{SA}\text{-N-S-Ti}_3\text{C}_2\text{T}_x$, which features smooth surfaces and edges (Figure 1c,d). No obvious Ru nanoparticle formation was observed in $\text{Ru}_{SA}\text{-N-S-Ti}_3\text{C}_2\text{T}_x$. Figure 1e displays a high-angle annular dark-field scanning transmission electron microscopy (HAADF-STEM) image of the $\text{Ru}_{SA}\text{-N-S-Ti}_3\text{C}_2\text{T}_x$ catalyst, in which the small, homogeneously distributed bright dots of < 1 nm in size confirm the presence of atomically dispersed Ru_{SA} isolated on the $\text{Ti}_3\text{C}_2\text{T}_x$ support. We estimated the ruthenium loading to be 1.2 wt% based on inductively coupled plasma-optical emission spectroscopy (ICP-OES) analysis. Furthermore, scanning transmission electron microscopy-energy dispersive X-ray (STEM-EDX) mapping shows the existence and uniform distribution of Ti, C, O, N, S, and Ru elements in the $\text{Ru}_{SA}\text{-N-S-Ti}_3\text{C}_2\text{T}_x$ catalyst (Figure 1f,g; the corresponding STEM-EDX profile is shown in Figure S2, Supporting Information). These results strongly suggest the homogeneous distribution of isolated Ru_{SA} in the $\text{Ru}_{SA}\text{-N-S-Ti}_3\text{C}_2\text{T}_x$ catalyst.

The X-ray diffraction (XRD) patterns of $\text{Ti}_3\text{C}_2\text{T}_x$ MXene show that a strong (002) peak is shifted to a lower angle ($2\theta = 9^\circ$) compared to that of the Ti_3AlC_2 starting material, suggesting the successful etching of Al layers from the MAX phase and the formation of the

MXene structure (Figure S3, Supporting Information).^[19] We performed X-ray photoelectron spectroscopy (XPS) and X-ray absorption fine structure spectroscopy (XAFS) to investigate the existence and electronic states of single Ru atoms in the Ru_{SA}-N-S-Ti₃C₂T_x catalyst. The existence of Ti, C, O and F elements in the survey scan indicates the successful preparation of the Ti₃C₂T_x MXene (Figure S4a, Supporting Information), which is further supported by the Ti-C bond observed in the high resolution C1s spectrum and the intense Ti³⁺ peak identified in the high resolution Ti2p spectrum (Figure S4b,c, Supporting Information). The survey scan spectra of the Ru_{SA}-N-S-Ti₃C₂T_x catalyst shows the presence of Ti, C, O, N, S, and Ru elements, indicating the doping of Ru, N, and S on the Ti₃C₂T_x MXene (Figure S5, Supporting Information). **Figure 2a** shows the high-resolution C1s and Ru3d XPS spectra of Ru_{SA}-N-S-Ti₃C₂T_x and a control made without Ru (N-S-Ti₃C₂T_x). The binding energy peaks identified for Ru_{SA}-N-S-Ti₃C₂T_x at 281.8 eV, 282.2 eV, 285.0 eV, 285.7 eV, 286.6 eV, and 288.4 eV correspond to C – Ti – N, C – Ti, graphitic C – C, C – N, C – O, and C=O, respectively.^[20] Compared with N-S-Ti₃C₂T_x, an additional small peak observed for Ru_{SA}-N-S-Ti₃C₂T_x at 280.6 eV located between the oxidation state of Ru(0) and Ru⁴⁺ indicates the different oxidation states of Ru in Ru_{SA}-N-S-Ti₃C₂T_x.^[21] Moreover, it is difficult to distinguish the Ru3d_{3/2} peak from the graphitic C-C signals because of spectral overlap in the energy range around 285.0 eV.^[21] The high-resolution N1s XPS spectrum of N-S-Ti₃C₂T_x shows peaks at 396.3 eV, 397.5 eV, 398.8 eV, and 399.4 eV, which are assigned to Ti–N, pyridinic – N, N – Ti – O, and pyrrolic – N bonds, respectively (Figure S6, Supporting Information).^[22,23] However, the pyrrolic-N component of Ru_{SA}-N-S-Ti₃C₂T_x is observed at 400.2 eV, which is ~0.8 eV higher than the pyrrolic–N of N-S-Ti₃C₂T_x (Figure 2b) possibly due to the chemical interaction between Ru_{SA} and the surrounding N atoms on the support.^[23] Meanwhile, the high resolution S2p spectrum of Ru_{SA}-N-S-Ti₃C₂T_x can be deconvoluted into six different components, including S–Ti (160.6 eV), chemisorbed S (161.8 eV), S–Ru (162.5

eV), S–C (163.8 eV and 165.0 eV), and sulfate species (168.0 eV) (Figure 2c).^{[24,25],[20]} The Ru–N bond and S–Ru bond identified in the high resolution N1s and high resolution S2p XPS results clearly confirm that the Ru_{SA} are coordinated with both N and S in Ru_{SA}-N-S-Ti₃C₂T_x. The Ti2p and Ru3p XPS spectra of Ru_{SA}-N-S-Ti₃C₂T_x are shown in Figure S7, Supporting Information. A binding energy peak identified at 455.1 eV is assigned to Ti–C bonds in Ti₃C₂T_x MXene.^[20] Two peaks located at 456.6 and 462.5 eV are related to the Ti³⁺ signal of Ti₃C₂T_x.^[20] In addition, the peaks at 455.7 eV, 458.8 eV, and 464.3 eV correspond to Ti–N, Ti–OH, and Ti–O bonds, respectively.^[20] A peak at 461.4 eV is attributed to Ru(0) or Ti²⁺.^[20,26]

To gain insight into the dispersion of Ru species on Ru_{SA}-N-S-Ti₃C₂T_x, we investigated the chemical state and coordination environment of the Ru_{SA} using X-ray absorption fine structure spectroscopy (XAFS). The Fourier Transform-X-ray absorption fine structure (FT-EXAFS) spectrum of Ru_{SA}-N-S-Ti₃C₂T_x exhibits a superimposed peak at 1.67 Å, which can be ascribed to both Ru–N(O) and Ru–S scattering pairs (Figure 2d). Compared to Ru foil and RuO₂, the absence of Ru–Ru and Ru–O scattering pairs in Ru_{SA}-N-S-Ti₃C₂T_x indicates the existence of atomically dispersed Ru_{SA} isolated on the MXene support (Figure 2d). Furthermore, we performed quantitative EXAFS curve fitting analysis to study the bonding environment of the Ru_{SA} (Figure 2e). As displayed in Table S1, Supporting Information, the coordination number of Ru–N(O) bonding in the first coordination bonding sphere is estimated to be 3.6 at a distance of 2.09 Å. Moreover, an additional coordination sphere with a coordination number of 1.1 at a distance of 2.37 Å corresponds to the Ru–S bonding configuration. These results confirm the successful coordination of Ru_{SA} with both N and S in Ru_{SA}-N-S-Ti₃C₂T_x, which is consistent with the XPS results. Figure 2f shows the normalized Ru k-edge X-ray absorption near edge structure (XANES) spectra of Ru foil, RuO₂, and Ru_{SA}-N-S-Ti₃C₂T_x. The Ru k-edge XANES profile of Ru_{SA}-N-S-Ti₃C₂T_x is

entirely different from those of the Ru foil and RuO₂ XANES profiles, indicating the different oxidation state of Ru_{SA} and further confirming the chemical coordination of Ru_{SA} with N and S species. Therefore, the EXAFS and XANES results confirm the strong electronic coupling between isolated Ru_{SA} and the Ti₃C₂T_x MXene support *via* N and S atoms.

Figure 3a shows the HER polarization curves of bare carbon paper (CP), Ti₃C₂T_x, N-S-Ti₃C₂T_x, Ru_{SA}-Ti₃C₂T_x, and Ru_{SA}-N-S-Ti₃C₂T_x catalysts in 0.5 M H₂SO₄ electrolyte. As shown in Figure 3a, the current densities of Ru_{SA}-Ti₃C₂T_x and Ru_{SA}-N-S-Ti₃C₂T_x catalysts are not in the baseline at zero overpotential, which might be due to the underpotential hydrogen adsorption effect of precious Ru metal and the capacitance effect of nanocarbons from Ti₃C₂T_x MXene support that influence the current starting points not at zero.^[27] The Ti₃C₂T_x, N-S-Ti₃C₂T_x, and Ru_{SA}-Ti₃C₂T_x catalysts feature large overpotential values of 673 mV, 453 mV, and 215 mV, respectively to reach a current density of 10 mA/cm². Remarkably, Ru_{SA}-N-S-Ti₃C₂T_x exhibits nearly zero onset potential (η_{onset}) and the smallest overpotentials of 76 mV and 237 mV to attain 10 mA/cm² and 100 mA/cm², respectively, indicating the exceptional electrocatalytic HER performance of Ru_{SA}-N-S-Ti₃C₂T_x, which we believe is due to the chemical interactions of the Ru_{SA} and MXene support. The Pt control sample exhibits the overpotential of 53 and 81 mV to reach the current densities of 10 and 100 mA/cm², respectively.

In order to study the effect of the heteroatom dual dopants (*i.e.*, N and S) on the HER performance, we prepared the same catalyst only doped with just N (*i.e.*, Ru_{SA}-N-Ti₃C₂T_x) under identical experimental conditions using urea as the N source for the control experiment. The Ru_{SA}-N-Ti₃C₂T_x has an overpotential of 151 mV at 10 mA/cm² (Figure S8, Supporting Information), which is ~75 mV higher than Ru_{SA}-N-S-Ti₃C₂T_x, indicating the improved catalytic performance when S atoms are also doped into the MXene substrate. The high

electronegativity and different atomic radii of the N and S atoms allows them to act as two different binding sites for the formation of the Ru_{SA} , which helps to drive the enhanced HER catalytic activity^[28]. We also studied the reaction kinetics of the catalysts during the HER process by extracting the slope values from the Tafel plots (Figure 3b). The Ru_{SA} -N-S- $\text{Ti}_3\text{C}_2\text{T}_x$ catalyst shows a Tafel slope of 90 mV dec^{-1} , suggesting that the Ru_{SA} -N-S- $\text{Ti}_3\text{C}_2\text{T}_x$ catalyst follows the Volmer-Heyrovsky mechanism that combines a fast initial discharge reaction step (Volmer reaction: $\text{H}_3\text{O}^+ + e^- \rightarrow \text{H}_{ads} + \text{H}_2\text{O}$) followed by a slow electrochemical desorption reaction step (Heyrovsky reaction: H

).^[29,30] A high Tafel value of 90 mV dec^{-1} noted for Ru_{SA} -N-S- $\text{Ti}_3\text{C}_2\text{T}_x$ could result from the $\text{Ti}_3\text{C}_2\text{T}_x$ MXene support. In contrast, this Tafel value is higher than the Tafel values of previously reported Ru-based electrocatalysts.^[21] However, the value is similar to those reported for MXene based HER catalyst [Ti_2CT_x (88 mV dec^{-1}) and Mo_2CT_x (82 mV dec^{-1})]^[31,32], suggesting that the HER active sites not only originate from Ru_{SA} but also arise from the electrochemically active $\text{Ti}_3\text{C}_2\text{T}_x$ MXene to some extent. We further evaluated the HER performance of Ru_{SA} -N-S- $\text{Ti}_3\text{C}_2\text{T}_x$ in alkaline and neutral pH electrolytes and found that overpotentials of 99 mV and 275 mV are required to achieve a current density of 10 mA/cm^2 , respectively, indicating the outstanding HER activity of the Ru_{SA} -N-S- $\text{Ti}_3\text{C}_2\text{T}_x$ catalyst under various pH conditions (Figure 3c,d). Figure 3e shows the electrochemical impedance spectra (EIS) of $\text{Ti}_3\text{C}_2\text{T}_x$, N-S- $\text{Ti}_3\text{C}_2\text{T}_x$, and Ru_{SA} -N-S- $\text{Ti}_3\text{C}_2\text{T}_x$ measured in 0.5 M H_2SO_4 . The Ru_{SA} -N-S- $\text{Ti}_3\text{C}_2\text{T}_x$ has a smaller charge transfer resistance than $\text{Ti}_3\text{C}_2\text{T}_x$ and N-S- $\text{Ti}_3\text{C}_2\text{T}_x$, which shows the HER process occurs effectively at the interface between the Ru_{SA} -N-S- $\text{Ti}_3\text{C}_2\text{T}_x$ surface and electrolyte.

The HER performance of Ru_{SA} -N-S- $\text{Ti}_3\text{C}_2\text{T}_x$ is retained up to 3000 cyclic voltammetry (CV) cycles with negligible negative shift ($\sim 17 \text{ mV}$) in the overpotential (Figure S9, Supporting Information), indicating the long-term stability of Ru_{SA} -N-S- $\text{Ti}_3\text{C}_2\text{T}_x$. In

addition, the resultant $\text{Ru}_{SA}\text{-N-S-Ti}_3\text{C}_2\text{T}_x$ catalyst provides excellent long-term stability in acidic electrolyte with negligible degradation in HER performance after 16 h of reaction time, which further reveals that the Ru_{SA} are well preserved on the MXene support (Figure S10, Supporting Information). Moreover, the $\text{Ru}_{SA}\text{-N-S-Ti}_3\text{C}_2\text{T}_x$ catalyst was also stable up to 4000 CV cycles and 1000 CV cycles under alkaline and neutral electrolytes, respectively (Figure S11a,b, Supporting Information). The EIS spectra of the $\text{Ru}_{SA}\text{-N-S-Ti}_3\text{C}_2\text{T}_x$ catalyst before and after CV cycling in alkaline and neutral electrolytes show only a slight increase in the charge transfer resistance even after several CV cycles (4000 cycles in alkaline electrolyte and 1000 cycles in neutral electrolyte) (Figure S11c,d, Supporting Information). The long-term chemical stability of $\text{Ru}_{SA}\text{-N-S-Ti}_3\text{C}_2\text{T}_x$ could be attributed to the thiourea-assisted carbonization that occurs during the synthesis of the $\text{Ru}_{SA}\text{-N-S-Ti}_3\text{C}_2\text{T}_x$ catalyst upon thermal annealing under inert atmosphere.^[33] The carbonization process largely prevents the MXene surface from oxidation and thereby preserves the MXene structure during the HER process.^[34] Moreover, the Ru_{SA} are strongly bonded with the MXene support via N and S binding sites, as evidenced from the XAFS results. Overall, the electrochemical results suggest that $\text{Ru}_{SA}\text{-N-S-Ti}_3\text{C}_2\text{T}_x$ is an efficient and stable electrocatalyst for HER.

To gain more insight into the enhanced HER performance, we calculated the double layer capacitance (C_{dl}) of the catalysts from the CV measurements obtained in 0.5 M H_2SO_4 . Figure 3f depicts the CV curves of $\text{Ru}_{SA}\text{-N-S-Ti}_3\text{C}_2\text{T}_x$ at different scan rates ranging from 5 to 100 mVs^{-1} . Similarly, the CV curves of $\text{Ti}_3\text{C}_2\text{T}_x$ at different scan rates are shown in Figure S12, Supporting Information. We determined the C_{dl} value of $\text{Ru}_{SA}\text{-N-S-Ti}_3\text{C}_2\text{T}_x$ to be 31 mF cm^{-2} , which is ~62-times higher than that of $\text{Ti}_3\text{C}_2\text{T}_x$ (0.5 mF cm^{-2}) (Figure 3g), indicating the high electrochemically active area with exposed catalytic active sites available on $\text{Ru}_{SA}\text{-N-S-Ti}_3\text{C}_2\text{T}_x$, which are favorable for boosting the HER performance. Turnover frequency (TOF) is an important factor used to evaluate the HER activity of a catalyst. We calculated the TOF

value of Ru_{SA}-N-S-Ti₃C₂T_x in 0.5 M H₂SO₄ electrolyte based on the ICP-OES analysis (TOF calculation details are provided in the Supplementary Information). Based on these results, we estimated the TOF values of Ru_{SA}-N-S-Ti₃C₂T_x at 100 mV, 150 mV, and 200 mV to be 0.52 s⁻¹, 0.87 s⁻¹, and 1.50 s⁻¹, respectively (Figure 3h). The TOF values of Ru_{SA}-N-S-Ti₃C₂T_x are comparable with reported transition metal-based HER catalysts in acidic electrolyte (Figure 3h)^[35-41], suggesting the exceptional activity of the catalyst.

To the best of our knowledge, this reported HER performance is superior to that of other MXene-based HER catalysts reported thus far (Table S2, Supporting Information). As shown in Figure 3i, the HER performance of Ru_{SA}-N-S-Ti₃C₂T_x is also comparable with many recently reported precious transition metals based HER electrocatalysts in acidic solution (Table S3, Supporting Information). For comparison, we prepared different metals (Fe, Co, Ni and Pt) anchored to the Ti₃C₂T_x MXene catalyst under the same experimental conditions and compared their HER performance to Ru_{SA}-N-S-Ti₃C₂T_x (Figure 3j). Among them, Ru_{SA}-N-S-Ti₃C₂T_x was found to be a superior HER catalyst, with the lowest overpotential value compared to that of Fe-N-S-Ti₃C₂T_x, Co-N-S-Ti₃C₂T_x, Ni-N-S-Ti₃C₂T_x, and Pt-N-S-Ti₃C₂T_x catalysts in acidic electrolyte. To understand the catalytic active sites in the Ru_{SA}-N-S-Ti₃C₂T_x electrocatalyst, we conducted a potassium thiocyanate ion (KSCN⁻) test in 0.5 M H₂SO₄. It is widely known that KSCN⁻ ions have the ability to block metal sites under acidic conditions.^[21,42] Therefore, we measured the HER polarization curves of the Ru_{SA}-N-S-Ti₃C₂T_x catalyst before and after the addition of KSCN⁻ ions to the 0.5 M H₂SO₄ electrolyte (Figure S13, Supporting Information). The addition of 40 mM KSCN⁻ ions increases the overpotential from 235 mV to 400 mV in order to reach a current density of 80 mA/cm². Further increasing the KSCN⁻ ion concentration to 80 mM does not further affect the performance, which indicates that all isolated metal sites were blocked by the KSCN⁻ ions. However, the overpotential achieved after KSCN⁻ addition is still lower than the

overpotential of $\text{Ti}_3\text{C}_2\text{T}_x$ MXene, suggesting that Ru_{SA} are not the sole source of active sites for the enhanced HER performance of the $\text{Ru}_{SA}\text{-N-S-Ti}_3\text{C}_2\text{T}_x$ catalyst. In order to further understand the effective role of $\text{Ti}_3\text{C}_2\text{T}_x$ as a potential support for HER, we used reduced graphene oxide (rGO) as an alternative substrate to anchor the Ru_{SA} . The Ru-N-S-rGO catalyst offers an overpotential of 231 mV at 10 mA/cm^2 , which is 155 mV higher overpotential than $\text{Ru}_{SA}\text{-N-S-Ti}_3\text{C}_2\text{T}_x$, suggesting the effective role of the MXene as a solid support for catalytic reactions (Figure S14, Supporting Information).

Based on our XPS and XAFS results, we performed density functional theory (DFT) calculations to better understand the fundamental mechanism and hydrogen binding energies of the $\text{Ru}_{SA}\text{-N-S-Ti}_3\text{C}_2\text{T}_x$ catalyst for HER. Figure S15, Supporting Information, shows the top and side view of the atomic model of a layer of $\text{Ti}_3\text{C}_2\text{T}_x$ that we used in our DFT calculations. In general, the hydrogen adsorption energy on a catalyst surface is a key descriptor for studying the HER catalytic performance, in which an ideal catalyst should possess an optimal hydrogen adsorption energy value close to that of Pt (*i.e.*, close to zero).^[43] The proposed atomic model of the $\text{Ru}_{SA}\text{-N-S-Ti}_3\text{C}_2\text{T}_x$ catalyst is illustrated in **Figure 4a**. The calculated energies of the catalysts are summarized in Table S4, Supporting Information. As shown in Figure 4b, the $\text{N-S-Ti}_3\text{C}_2\text{T}_x$, $\text{Ru}_{SA}\text{-Ti}_3\text{C}_2\text{T}_x$, and $\text{Ru}_{SA}\text{-N-Ti}_3\text{C}_2\text{T}_x$ catalysts offer largely negative Gibbs hydrogen adsorption free energy (ΔG_{H^*}) values of -0.86 eV, -0.41 eV, and -0.25 eV, respectively, indicating the strong H adsorption behaviour on these catalysts and thus the high energy barriers for the formation and desorption of H_2 . Impressively, $\text{Ru}_{SA}\text{-N-S-Ti}_3\text{C}_2\text{T}_x$ achieves an optimal ΔG_{H^*} value of 0.08 eV, which is much closer to zero, highlighting the favourable H adsorption-desorption and subsequent H_2 production characteristics of $\text{Ru}_{SA}\text{-N-S-Ti}_3\text{C}_2\text{T}_x$, enabling it to effectively drive the overall HER process. The optimal ΔG_{H^*} achieved by the $\text{Ru}_{SA}\text{-N-S-Ti}_3\text{C}_2\text{T}_x$ catalyst could be attributed to the chemical interaction between the Ru_{SA} and MXene support, as evidenced

from the XAFS results. Figure S16, Supporting Information, shows the partial density of states (PDOS) of Ru_{SA} in Ru_{SA}-Ti₃C₂T_x, Ru_{SA}-N-Ti₃C₂T_x, and Ru_{SA}-N-S-Ti₃C₂T_x. The yellow regions of the PDOS diagrams show how doping of Ru_{SA} induces charge transfer between the Ru_{SA} and MXene and thereby creates non-bonding states around the Fermi energy level. The lower intensity of the non-bonding states and change in density of states indicate that the isolated Ru atoms optimize the catalytic activity, which matches the trend of ΔG_{H^*} . Furthermore, the total density of states (TDOS) analysis confirms that Ti₃C₂T_x can be used as a solid support with good electronic conductivity. As depicted in Figure 4c, the TDOS of Ti₃C₂T_x, N-S-Ti₃C₂T_x, Ru_{SA}-Ti₃C₂T_x, Ru_{SA}-N-Ti₃C₂T_x, and Ru_{SA}-N-S-Ti₃C₂T_x demonstrates that all the systems possess metallic characteristics, which is beneficial for the electrocatalytic HER. Overall the DFT results strongly suggest that the decoration of Ru_{SA} onto the MXene support alters the electronic structure of Ru_{SA} with optimal ΔG_{H^*} to effectively facilitate the HER process.

Photoelectrochemical (PEC) water splitting is one of the economically viable approaches for producing clean solar hydrogen.^[44,45] We integrated the Ti₃C₂T_x and Ru_{SA}-N-S-Ti₃C₂T_x electrocatalysts with n^+np^+ -Si photocathode to evaluate their PEC H₂ production performance (see more details on PEC measurements in the Methods). The PEC device structure of the Ru_{SA}-N-S-Ti₃C₂T_x/ n^+np^+ -Si photocathode is shown in **Figure 5a**. It has been previously shown that the drop casting of Ti₃C₂T_x MXene can easily form a Schottky junction with n -Si by just van der Waals forces.^[46] Therefore, we were able to directly drop cast the Ru_{SA}-N-S-Ti₃C₂T_x catalyst onto the n^+ side of the Si photocathode. The work function and band alignment of Ru_{SA}-N-S-Ti₃C₂T_x/ n^+np^+ -Si photocathode were investigated using ultraviolet photoelectron spectroscopy (UPS) (Figure S17, Supporting Information). The secondary electron cut-off energy obtained from the UPS spectra can be subtracted from the incident UV photon energy (He I excitation energy of 21.21 eV) to calculate the work

function of the materials.^[46] In case of n^+np^+ -Si, the secondary electron cut-off energy is 17.26 eV and its corresponding work function is calculated to be $21.21-17.26$ eV = 3.95 eV (the inset in Figure S17, Supporting Information). However, the secondary electron cut-off energy of $\text{Ru}_{SA}\text{-N-S-Ti}_3\text{C}_2\text{T}_x$ shift towards low binding energy (16.96 eV) compared to n^+np^+ -Si, the work function of $\text{Ru}_{SA}\text{-N-S-Ti}_3\text{C}_2\text{T}_x$ is estimated to be $21.21-16.96$ eV = 4.25 eV that is higher than the work function of n^+np^+ -Si. Moreover, the work function of $\text{Ru}_{SA}\text{-N-S-Ti}_3\text{C}_2\text{T}_x$ catalyst is comparable with the previously reported work function values for $\text{Ti}_3\text{C}_2\text{T}_x$ MXene.^[46,47] Based on the work functions, we proposed the band structure diagram for $\text{Ru}_{SA}\text{-N-S-Ti}_3\text{C}_2\text{T}_x/n^+np^+$ -Si photocathode (Figure 5b). As shown in Figure 5b, upon light illumination, the photogenerated electrons from n^+np^+ -Si photocathode can promptly migrate to the $\text{Ru}_{SA}\text{-N-S-Ti}_3\text{C}_2\text{T}_x$ catalyst surface because of their difference in the work functions. Thus, the continuous shuttle of these photogenerated electrons to the active sites of $\text{Ru}_{SA}\text{-N-S-Ti}_3\text{C}_2\text{T}_x$ catalyst can prevents the charge carrier recombination on Si and Si/ $\text{Ru}_{SA}\text{-N-S-Ti}_3\text{C}_2\text{T}_x$ interface and thereby efficiently enhances the PEC H_2 production performance. Figure 5c-e displays SEM images of the p^+ - and n^+ -Si surfaces of the device, as well as the n^+ -Si side after the deposition of the $\text{Ru}_{SA}\text{-N-S-Ti}_3\text{C}_2\text{T}_x$ catalyst. The n^+ -Si surface of the photocathode features micropyramidal structures for improved light absorption, while the p^+ -Si surface is grooved (Figure 5c,d.) The SEM image of the $\text{Ru}_{SA}\text{-N-S-Ti}_3\text{C}_2\text{T}_x/n^+np^+$ -Si photocathode clearly shows that the $\text{Ru}_{SA}\text{-N-S-Ti}_3\text{C}_2\text{T}_x$ catalyst uniformly coats the grooved surface of the n^+np^+ -Si (Figure 5e). Figure 5f displays the current density-voltage (J-V) characteristic curves of the $\text{Ti}_3\text{C}_2\text{T}_x/n^+np^+$ -Si and $\text{Ru}_{SA}\text{-N-S-Ti}_3\text{C}_2\text{T}_x/n^+np^+$ -Si photocathodes under dark and illuminated conditions. Upon AM 1.5G illumination, the $\text{Ti}_3\text{C}_2\text{T}_x/n^+np^+$ -Si photocathode exhibits a photocurrent density of 3.7 mA/cm²@ 1 mA/cm² and an onset potential of 82 mV vs. RHE. Remarkably, the $\text{Ru}_{SA}\text{-N-S-Ti}_3\text{C}_2\text{T}_x/n^+np^+$ -Si photocathode exhibits an onset potential of 455 mV vs. RHE @ 1 mA/cm² and a photocurrent density of

37.6 mA/cm², which is ~10-times higher than the photocurrent density of the Ti₃C₂T_x/n⁺np⁺-Si photocathode. The long-term stability of Ru_{SA}-N-S-Ti₃C₂T_x/n⁺np⁺-Si photocathode is evaluated in 0.5 M H₂SO₄ electrolyte under AM 1.5G illumination (Figure S18, Supporting Information). The photocurrent density gradually decreases with respect to the reaction time, which might be due to the gradual removal of Ru_{SA}-N-S-Ti₃C₂T_x catalyst from n⁺np⁺-Si surface during PEC H₂ production reaction. The outstanding PEC performance of the Ru_{SA}-N-S-Ti₃C₂T_x/n⁺np⁺-Si photocathode is due to the excellent HER activity of the Ru_{SA}-N-S-Ti₃C₂T_x electrocatalyst. As shown in Figure 5g, the photocurrent density value of Ru_{SA}-N-S-Ti₃C₂T_x/n⁺np⁺-Si photocathode is even better than most transition metals and earth abundant HER catalysts integrated on Si-based photocathodes reported thus far (Table S5, Supporting Information). In addition, the onset potential of the Ru_{SA}-N-S-Ti₃C₂T_x/n⁺np⁺-Si photocathode is comparable with most reported transition metals and earth abundant HER electrocatalysts coupled to Si photocathodes (Figure 5h, Table S5, Supporting Information). The PEC results shown herein demonstrate that the integration of a hydrophilic and electrically conductive MXene-based electrocatalyst with a Si photocathode could provide a scalable approach towards developing high performance Si photocathodes for solar-driven PEC water splitting applications.

In summary, we have demonstrated that Ru_{SA}-N-S-Ti₃C₂T_x is an efficient and stable HER electrocatalyst. The HER performance of Ru_{SA}-N-S-Ti₃C₂T_x is superior than other previously reported MXene-based HER catalysts and most transition-metal-based HER catalysts. XAFS and DFT simulation studies reveal that the remarkable HER catalytic activity of Ru_{SA}-N-S-Ti₃C₂T_x is mainly due to the catalytically active interfaces of the Ru_{SA}-Ti₃C₂T_x MXene support and its optimal ΔG_{H^*} value. Furthermore, incorporating the Ru_{SA}-N-S-Ti₃C₂T_x catalyst into a n⁺np⁺-Si photocathode significantly boosts the photocurrent density to

37.6 mA/cm², which is ~10-times higher than that of the Ti₃C₂T_x/n⁺np⁺-Si photocathode. Both experimental and theoretical studies clearly demonstrate that the catalytic properties of MXenes can be tailored via metal-support interactions.

Supporting Information

Supporting Information is available from the Wiley Online Library or from the author

Acknowledgements

This work was supported by the King Abdullah University of Science and Technology (KAUST). We acknowledge the startup fund of City University of Hong Kong. We thank the Australian Research Council for funding this work under the Discovery Grant program. This research was undertaken on the supercomputers in the National Computational Infrastructure (NCI) in Canberra, Australia, which is supported by the Australian Commonwealth Government, and the Pawsey Supercomputing Centre in Perth with funding from the Australian government and the Government of Western Australia.

Conflict of Interest

The authors declare no conflict of interest.

Keywords

Single atom catalyst, MXene, Work Function, Photocathode, Hydrogen evolution

References

- [1] A. Wang, J. Li, T. Zhang, *Nat. Rev. Chem.* **2018**, *2*, 65.
- [2] Z. Luo, Y. Ouyang, H. Zhang, M. Xiao, J. Ge, Z. Jiang, J. Wang, D. Tang, X. Cao, C. Liu, W. Xing, *Nat. Commun.* **2018**, *9*, 2120.
- [3] A. Alarawi, V. Ramalingam, J.-H. He, *Mater. Today Energy* **2019**, *11*, 1.
- [4] H. Wei, X. Liu, A. Wang, L. Zhang, B. Qiao, X. Yang, Y. Huang, S. Miao, J. Liu, T. Zhang, *Nat. Commun.* **2014**, *5*, 5634.
- [5] L. Nie, D. Mei, H. Xiong, B. Peng, Z. Ren, X. I. P. Hernandez, A. DeLaRiva, M. Wang, M. H. Engelhard, L. Kovarik, A. K. Datye, Y. Wang, *Science* **2017**, *358*, 1419.
- [6] M. Dhiman, V. Polshettiwar, *ChemCatChem* **2018**, *10*, 881.
- [7] Y. Chen, S. Ji, C. Chen, Q. Peng, D. Wang, Y. Li, *Joule* **2018**, *2*, 1242.
- [8] D. A. C. Brownson, S. A. Varey, F. Hussain, S. J. Haigh, C. E. Banks, *Nanoscale* **2014**, *6*, 1607.
- [9] J. Yang, B. Chen, X. Liu, W. Liu, Z. Li, J. Dong, W. Chen, W. Yan, T. Yao, X. Duan, Y. Yu, Y. Li, *Angew. Chemie Int. Ed.* **2018**, *57*, 9495.
- [10] M. Ghidui, M. R. Lukatskaya, M.-Q. Zhao, Y. Gogotsi, M. W. Barsoum, *Nature* **2014**, *516*, 78.
- [11] H. Fu, V. Ramalingam, H. Kim, C. Lin, X. Fang, H. N. Alshareef, J. He, *Adv. Energy Mater.* **2019**, 1900180.
- [12] J. Pang, R. G. Mendes, A. Bachmatiuk, L. Zhao, H. Q. Ta, T. Gemming, H. Liu, Z. Liu, M. H. Rummeli, *Chem. Soc. Rev.* **2019**, *48*, 72.
- [13] C. Zhu, Q. Shi, S. Feng, D. Du, Y. Lin, *ACS Energy Lett.* **2018**, *3*, 1713.
- [14] M. R. Lukatskaya, S. Kota, Z. Lin, M.-Q. Zhao, N. Shpigel, M. D. Levi, J. Halim, P.-L. Taberna, M. W. Barsoum, P. Simon, Y. Gogotsi, *Nat. Energy* **2017**, *2*, 17105.
- [15] Z. Li, Y. Cui, Z. Wu, C. Milligan, L. Zhou, G. Mitchell, B. Xu, E. Shi, J. T. Miller, F. H. Ribeiro, Y. Wu, *Nat. Catal.* **2018**, *1*, 349.
- [16] Z. Li, L. Yu, C. Milligan, T. Ma, L. Zhou, Y. Cui, Z. Qi, N. Libretto, B. Xu, J. Luo, E. Shi, Z. Wu, H. Xin, W. N. Delgass, J. T. Miller, Y. Wu, *Nat. Commun.* **2018**, *9*, 5258.
- [17] J. Zhang, Y. Zhao, X. Guo, C. Chen, C.-L. Dong, R.-S. Liu, C.-P. Han, Y. Li, Y. Gogotsi, G. Wang, *Nat. Catal.* **2018**, *1*, 985.
- [18] C. Zhang, J. Sha, H. Fei, M. Liu, S. Yazdi, J. Zhang, Q. Zhong, X. Zou, N. Zhao, H. Yu, Z. Jiang, E. Ringe, B. I. Yakobson, J. Dong, D. Chen, J. M. Tour, *ACS Nano* **2017**, *11*, 6930.
- [19] J. Ran, G. Gao, F.-T. Li, T.-Y. Ma, A. Du, S.-Z. Qiao, *Nat. Commun.* **2017**, *8*, 13907.

- [20] W. Bao, L. Liu, C. Wang, S. Choi, D. Wang, G. Wang, *Adv. Energy Mater.* **2018**, *8*, 1702485.
- [21] J. Mahmood, F. Li, S.-M. Jung, M. S. Okyay, I. Ahmad, S.-J. Kim, N. Park, H. Y. Jeong, J.-B. Baek, *Nat. Nanotechnol.* **2017**, *12*, 441.
- [22] Y. Wen, T. E. Rufford, X. Chen, N. Li, M. Lyu, L. Dai, L. Wang, *Nano Energy* **2017**, *38*, 368.
- [23] J. Su, Y. Yang, G. Xia, J. Chen, P. Jiang, Q. Chen, *Nat. Commun.* **2017**, *8*, 14969.
- [24] X. Zhang, Z. Luo, P. Yu, Y. Cai, Y. Du, D. Wu, S. Gao, C. Tan, Z. Li, M. Ren, T. Osipowicz, S. Chen, Z. Jiang, J. Li, Y. Huang, J. Yang, Y. Chen, C. Y. Ang, Y. Zhao, P. ang, L. Song, X. Wu, Z. Liu, A. Borgna, H. Zhang, *Nat. Catal.* **2018**, *1*, 460.
- [25] R. Demir-Cakan, M. Morcrette, F. Nouar, C. Davoisne, T. Devic, D. Gonbeau, R. Dominko, C. Serre, G. Férey, J.-M. Tarascon, *J. Am. Chem. Soc.* **2011**, *133*, 16154.
- [26] S. Liu, Q. Liu, Y. Lv, B. Chen, Q. Zhou, L. Wang, Q. Zheng, C. Che, C. Chen, *Chem. Commun.* **2017**, *53*, 13153.
- [27] Y. Zheng, Y. Jiao, Y. Zhu, L. H. Li, Y. Han, Y. Chen, M. Jaroniec, S.-Z. Qiao, *J. Am. Chem. Soc.* **2016**, *138*, 16174.
- [28] Q. Li, W. Chen, H. Xiao, Y. Gong, Z. Li, L. Zheng, X. Zheng, W. Yan, W.-C. Cheong, R. Shen, N. Fu, L. Gu, Z. Zhuang, C. Chen, D. Wang, Q. Peng, J. Li, Y. Li, *Adv. Mater.* **2018**, *30*, 1800588.
- [29] J. Kibsgaard, T. F. Jaramillo, F. Besenbacher, *Nat. Chem.* **2014**, *6*, 248.
- [30] W. Yuan, L. Cheng, Y. An, H. Wu, N. Yao, X. Fan, X. Guo, *ACS Sustain. Chem. Eng.* **2018**, *6*, 8976.
- [31] Z. W. Seh, K. D. Fredrickson, B. Anasori, J. Kibsgaard, A. L. Strickler, M. R. Lukatskaya, Y. Gogotsi, T. F. Jaramillo, A. Vojvodic, *ACS Energy Lett.* **2016**, *1*, 589.
- [32] A. D. Handoko, K. D. Fredrickson, B. Anasori, K. W. Convey, L. R. Johnson, Y. Gogotsi, A. Vojvodic, Z. W. Seh, *ACS Appl. Energy Mater.* **2018**, *1*, 173.
- [33] X. Wu, Z. Wang, M. Yu, L. Xiu, J. Qiu, *Adv. Mater.* **2017**, *29*, 1607017.
- [34] C. Yang, W. Que, Y. Tang, Y. Tian, X. Yin, *J. Electrochem. Soc.* **2017**, *164*, A1939.
- [35] J. Yin, Q. Fan, Y. Li, F. Cheng, P. Zhou, P. Xi, S. Sun, *J. Am. Chem. Soc.* **2016**, *138*, 14546.
- [36] H.-W. Liang, S. Brüller, R. Dong, J. Zhang, X. Feng, K. Müllen, *Nat. Commun.* **2015**, *6*, 7992.
- [37] H. Fei, J. Dong, M. J. Arellano-Jiménez, G. Ye, N. Dong Kim, E. L. G. Samuel, Z. Peng, Z. Zhu, F. Qin, J. Bao, M. J. Yacaman, P. M. Ajayan, D. Chen, J. M. Tour, *Nat. Commun.* **2015**, *6*, 8668.
- [38] H.-J. Qiu, Y. Ito, W. Cong, Y. Tan, P. Liu, A. Hirata, T. Fujita, Z. Tang, M. Chen, *Angew. Chemie Int. Ed.* **2015**, *54*, 14031.

- [39] W. Chen, J. Pei, C.-T. He, J. Wan, H. Ren, Y. Zhu, Y. Wang, J. Dong, S. Tian, W.-C. Cheong, S. Lu, L. Zheng, X. Zheng, W. Yan, Z. Zhuang, C. Chen, Q. Peng, D. Wang, Y. Li, *Angew. Chemie Int. Ed.* **2017**, *56*, 16086.
- [40] Z. Fang, L. Peng, Y. Qian, X. Zhang, Y. Xie, J. J. Cha, G. Yu, *J. Am. Chem. Soc.* **2018**, *140*, 5241.
- [41] J. R. McKone, B. F. Sadtler, C. A. Werlang, N. S. Lewis, H. B. Gray, *ACS Catal.* **2013**, *3*, 166.
- [42] H. Zhang, P. An, W. Zhou, B. Y. Guan, P. Zhang, J. Dong, X. W. (David) Lou, *Sci. Adv.* **2018**, *4*, eaao6657.
- [43] J. Xu, T. Liu, J. Li, B. Li, Y. Liu, B. Zhang, D. Xiong, I. Amorim, W. Li, L. Liu, *Energy Environ. Sci.* **2018**, *11*, 1819.
- [44] G. Huang, R. Fan, X. Zhou, Z. Xu, W. Zhou, W. Dong, M. Shen, *Chem. Commun.* **2019**, *55*, 377.
- [45] A. Alarawi, V. Ramalingam, H.-C. Fu, P. Varadhan, R. Yang, J.-H. He, *Opt. Express* **2019**, *27*, A352.
- [46] Z. Kang, Y. Ma, X. Tan, M. Zhu, Z. Zheng, N. Liu, L. Li, Z. Zou, X. Jiang, T. Zhai, Y. Gao, *Adv. Electron. Mater.* **2017**, *3*, 1700165.
- [47] T. Schultz, N. C. Frey, K. Hantanasirisakul, S. Park, S. J. May, V. B. Shenoy, Y. Gogotsi, N. Koch, *Chem. Mater.* **2019**, *31*, 6590.

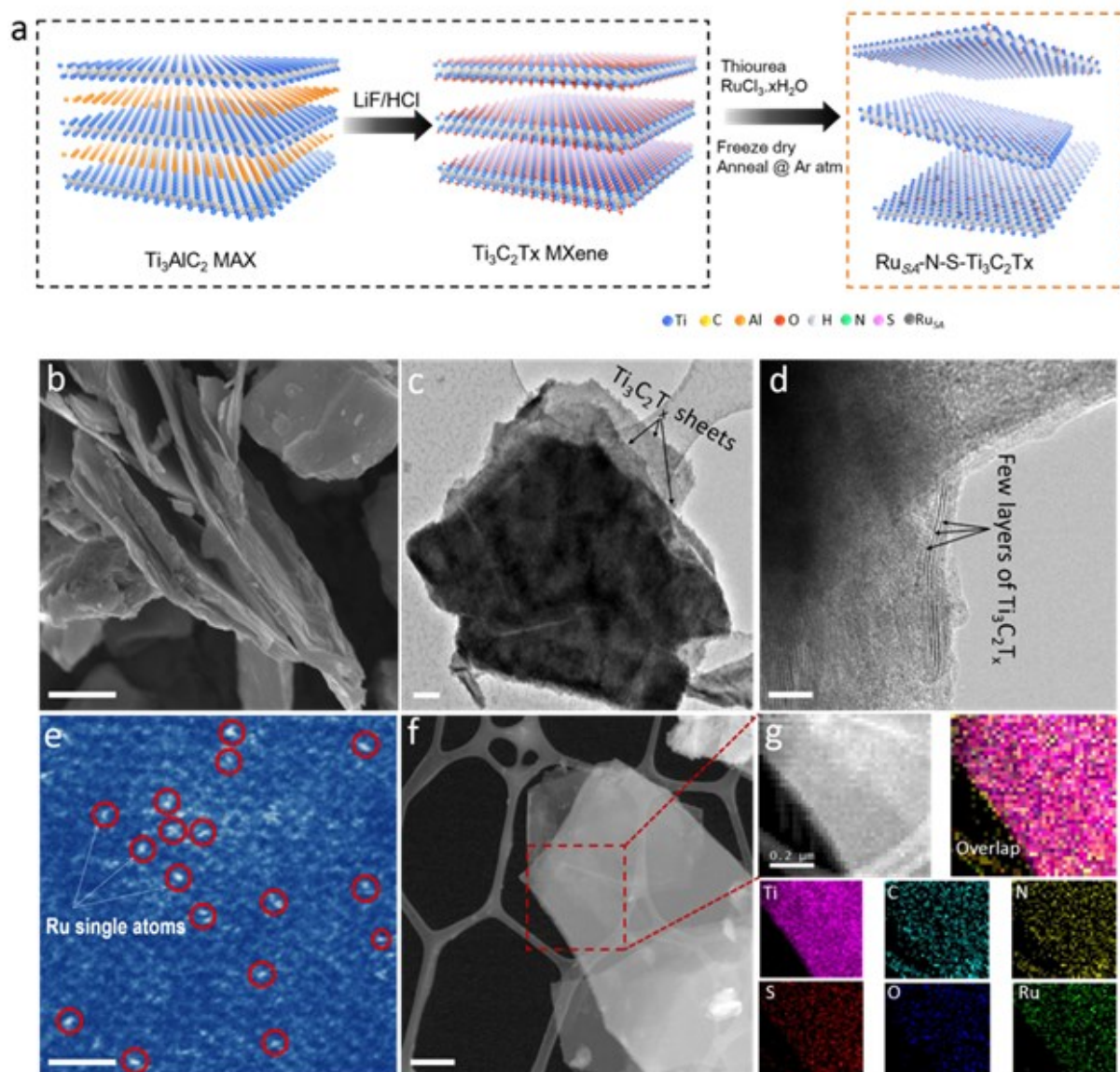


Figure 1. Synthesis and morphological characterizations of the $\text{Ru}_{\text{SA}}\text{-N-S-Ti}_3\text{C}_2\text{T}_x$ catalyst. a) Schematic illustration of the $\text{Ru}_{\text{SA}}\text{-N-S-Ti}_3\text{C}_2\text{T}_x$ catalyst synthetic route: $\text{Ti}_3\text{C}_2\text{T}_x$ was synthesized from MAX phase Ti_3AlC_2 using a LiF/HCl mixture. Doping of N, S, and Ru_{SA} on the $\text{Ti}_3\text{C}_2\text{T}_x$ was achieved by a freeze-drying process, followed by thermal annealing under Ar atmosphere. b) FE-SEM image of $\text{Ru}_{\text{SA}}\text{-N-S-Ti}_3\text{C}_2\text{T}_x$ demonstrates the stacked nanosheet morphology. Scale bar, 500 nm. c) TEM image of $\text{Ru}_{\text{SA}}\text{-N-S-Ti}_3\text{C}_2\text{T}_x$ shows the 2D $\text{Ti}_3\text{C}_2\text{T}_x$ nanosheets. Scale bar, 200 nm. d) High resolution-TEM image of few layered $\text{Ru}_{\text{SA}}\text{-N-S-Ti}_3\text{C}_2\text{T}_x$, Scale bar, 20 nm. e) Magnified HAADF-STEM image of $\text{Ru}_{\text{SA}}\text{-N-S-Ti}_3\text{C}_2\text{T}_x$ (bright dots marked with red circles indicate the Ru_{SA} on the $\text{Ti}_3\text{C}_2\text{T}_x$ MXene support). Scale bar, 2 nm. f) STEM image of $\text{Ru}_{\text{SA}}\text{-N-S-Ti}_3\text{C}_2\text{T}_x$, scale care, 200 μm and g) the corresponding elemental maps of titanium, carbon, nitrogen, sulfur, oxygen, and ruthenium elements found in $\text{Ru}_{\text{SA}}\text{-N-S-Ti}_3\text{C}_2\text{T}_x$.

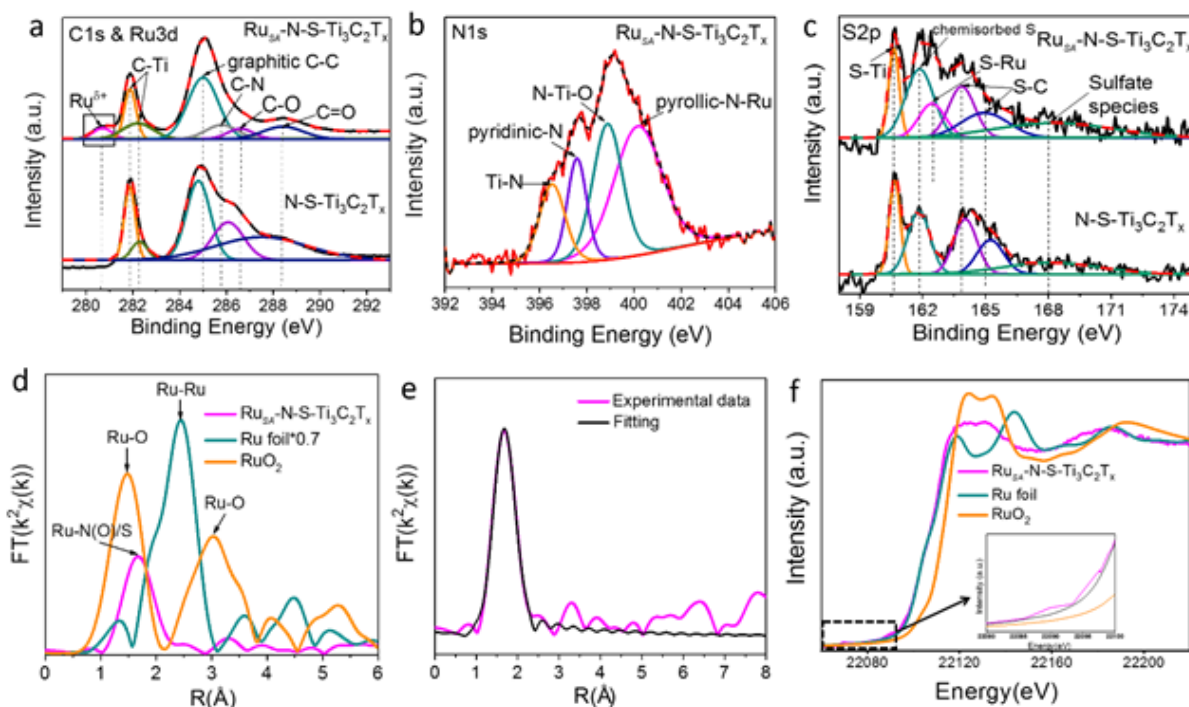


Figure 2. Chemical state and coordination environment of Ru single atoms in the $\text{Ru}_{\text{SA}}\text{-N-S-Ti}_3\text{C}_2\text{T}_x$ catalyst. a) High resolution C1s and Ru3d XPS spectra of $\text{N-S-Ti}_3\text{C}_2\text{T}_x$ and $\text{Ru}_{\text{SA}}\text{-N-S-Ti}_3\text{C}_2\text{T}_x$. b) High resolution N1s XPS spectrum of $\text{Ru}_{\text{SA}}\text{-N-S-Ti}_3\text{C}_2\text{T}_x$. c) High resolution S2p XPS spectra of $\text{N-S-Ti}_3\text{C}_2\text{T}_x$ and $\text{Ru}_{\text{SA}}\text{-N-S-Ti}_3\text{C}_2\text{T}_x$. d) The FT-EXAFS spectra of Ru foil shows a main Ru-Ru peak at 2.44 Å (which corresponds to the Ru-Ru shell with a coordination number of 2.68 Å, based on fitting), while RuO_2 displays two peaks at 1.47 Å and 3.0 Å (which correspond to the Ru-O shell with coordination numbers of 1.90 Å and 2.02 Å, respectively, based on fitting) and $\text{Ru}_{\text{SA}}\text{-N-S-Ti}_3\text{C}_2\text{T}_x$ shows a Ru-N(O)/S peak at 1.67 Å (which corresponds to the Ru-N/O and Ru-S shells with the coordination numbers of 2.09 Å and 2.37 Å, respectively, based on fitting). e) Quantitative EXAFS curve fitting at r-space for $\text{Ru}_{\text{SA}}\text{-N-S-Ti}_3\text{C}_2\text{T}_x$. f) The normalized Ru k-edge XANES spectra of Ru foil, RuO_2 , and $\text{Ru}_{\text{SA}}\text{-N-S-Ti}_3\text{C}_2\text{T}_x$.

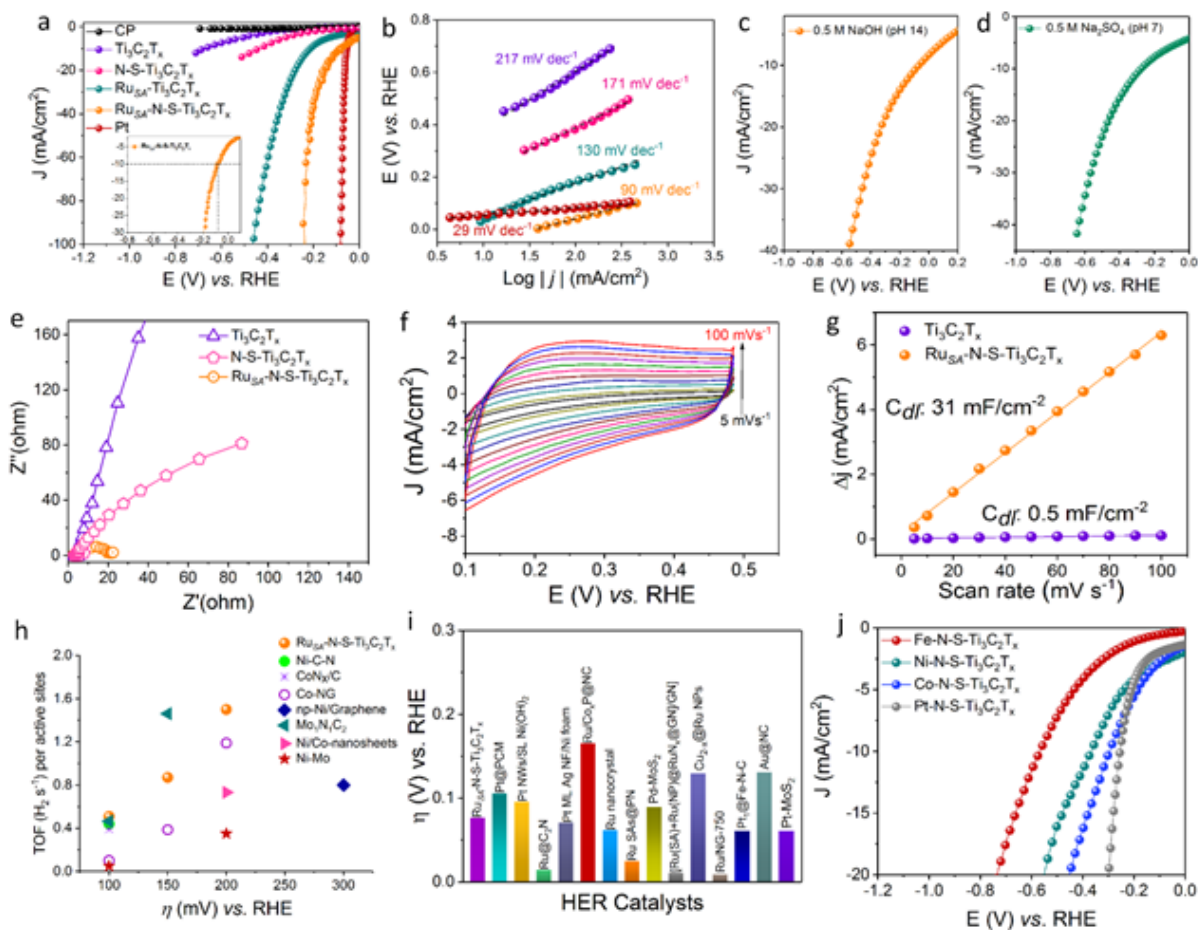


Figure 3. Electrochemical HER performance of the $\text{Ru}_{\text{SA}}\text{-N-S-Ti}_3\text{C}_2\text{T}_x$ catalyst. a) HER polarization curves of bare carbon paper (CP), $\text{Ti}_3\text{C}_2\text{T}_x$, N-S- $\text{Ti}_3\text{C}_2\text{T}_x$, $\text{Ru}_{\text{SA}}\text{-Ti}_3\text{C}_2\text{T}_x$, Pt and $\text{Ru}_{\text{SA}}\text{-N-S-Ti}_3\text{C}_2\text{T}_x$ catalysts recorded in 0.5 M H_2SO_4 . Inset: the magnified view of the HER polarization curve of $\text{Ru}_{\text{SA}}\text{-N-S-Ti}_3\text{C}_2\text{T}_x$. b) The Tafel plots corresponding to part (a). c,d) HER polarization curves of $\text{Ru}_{\text{SA}}\text{-N-S-Ti}_3\text{C}_2\text{T}_x$ in c) 0.5 M NaOH and d) 0.5 M Na_2SO_4 . e) EIS spectra of $\text{Ti}_3\text{C}_2\text{T}_x$, N-S- $\text{Ti}_3\text{C}_2\text{T}_x$, and $\text{Ru}_{\text{SA}}\text{-N-S-Ti}_3\text{C}_2\text{T}_x$. f) CV curves of the $\text{Ru}_{\text{SA}}\text{-N-S-Ti}_3\text{C}_2\text{T}_x$ electrocatalyst obtained at different scan rates in 0.5 M H_2SO_4 . g) Current density difference ($\Delta j = j_{\text{a}} - j_{\text{c}}$) plot of $\text{Ti}_3\text{C}_2\text{T}_x$ and $\text{Ru}_{\text{SA}}\text{-N-S-Ti}_3\text{C}_2\text{T}_x$ electrocatalysts at 0.27 V vs. RHE as a function of different scan rates to calculate the double layer capacitance value (C_{dl}). h) TOF of the $\text{Ru}_{\text{SA}}\text{-N-S-Ti}_3\text{C}_2\text{T}_x$ catalyst compared to previously reported metal-based HER electrocatalysts. i) Overpotential comparison of $\text{Ru}_{\text{SA}}\text{-N-S-Ti}_3\text{C}_2\text{T}_x$ with recently reported precious transition-metal-based HER electrocatalysts in acidic electrolyte. j) HER polarization curves of the Fe-N-S- $\text{Ti}_3\text{C}_2\text{T}_x$, Ni-N-S- $\text{Ti}_3\text{C}_2\text{T}_x$, Co-N-S- $\text{Ti}_3\text{C}_2\text{T}_x$, and Pt-N-S- $\text{Ti}_3\text{C}_2\text{T}_x$ electrocatalysts in 0.5 M H_2SO_4 .

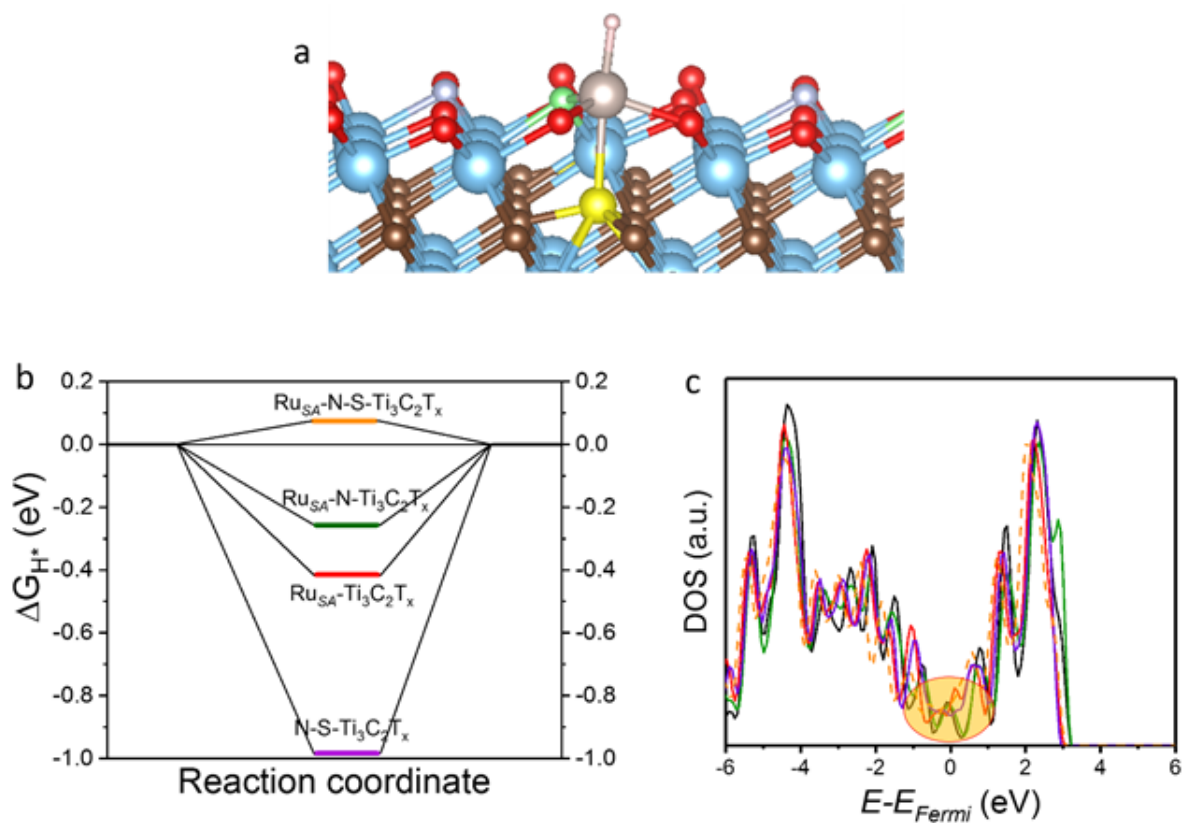


Figure 4. Density functional theory (DFT) calculation studies. a) Atomic model of the Ru_{S_A}-N-S-Ti₃C₂T_x catalyst (blue, brown, red, light blue, yellow, green, and grey colored balls represent Ti, C, O, F, S, N, and Ru atoms, respectively). b) The calculated Gibbs hydrogen adsorption free energy (ΔG_{H^*}) diagram of the N-S-Ti₃C₂T_x, Ru_{S_A}-Ti₃C₂T_x, Ru_{S_A}-N-Ti₃C₂T_x, and Ru_{S_A}-N-S-Ti₃C₂T_x catalysts. c) The total density of states (TDOS) of Ti₃C₂T_x (black line), N-S-Ti₃C₂T_x (violet line), Ru_{S_A}-Ti₃C₂T_x (red line), Ru_{S_A}-N-Ti₃C₂T_x (green line), and Ru_{S_A}-N-S-Ti₃C₂T_x (orange dashed line).

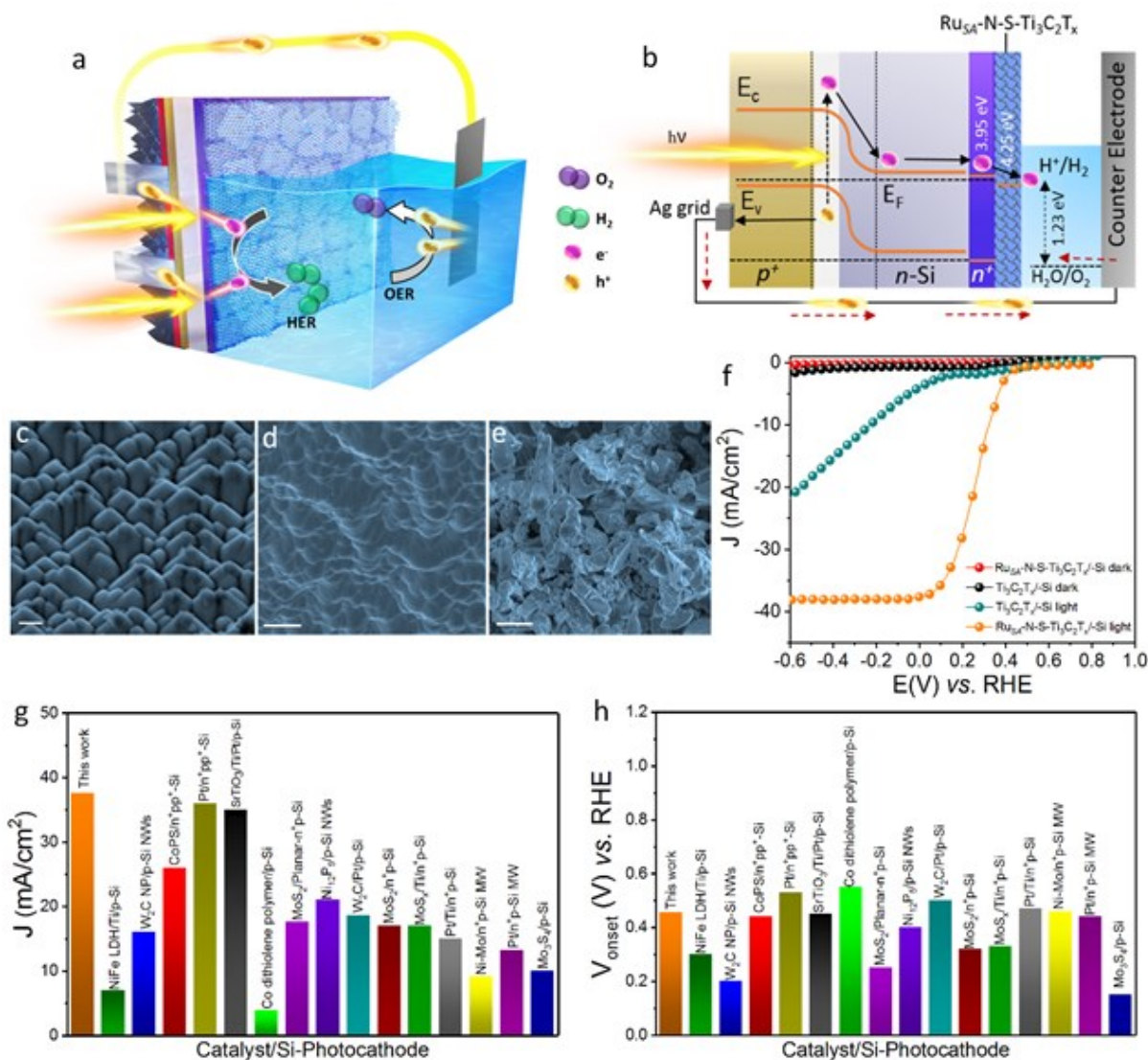
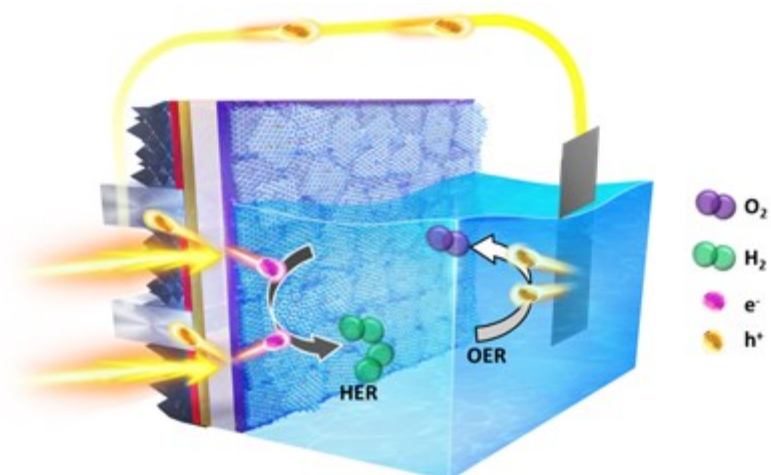


Figure 5. PEC H₂ production performance of the Ru_{SA}-N-S-Ti₃C₂T_x catalyst integrated with n⁺np⁺-Si photocathode. a) The Ru_{SA}-N-S-Ti₃C₂T_x/n⁺np⁺-Si photocathode device structure. b) Band structure diagram of the Ru_{SA}-N-S-Ti₃C₂T_x/n⁺np⁺-Si photocathode. c) SEM image of the n⁺ side of the n⁺np⁺-Si; scale bar, 10 μm. d) p⁺ side of the n⁺np⁺-Si; scale bar, 5 μm. e) Ru_{SA}-N-S-Ti₃C₂T_x coated on the n⁺ side of the Si photocathode; scale bar, 5 μm. f) current density-voltage (J-V) characteristic curves of the Ti₃C₂T_x and Ru_{SA}-N-S-Ti₃C₂T_x electrocatalysts integrated on the n⁺np⁺-Si photocathode (0.5 M H₂SO₄, scan rate: 20 mV/s, AM 1.5 illumination). Comparison of the g) photocurrent density and h) onset potential of the Ru_{SA}-N-S-Ti₃C₂T_x/n⁺np⁺-Si photocathode with previously reported earth-abundant and transition-metal-based electrocatalysts integrated with Si-based photocathodes.



Ti₃C₂T_x MXene is demonstrated as a 2D solid support to host Ruthenium single atom (Ru_{SA}) catalyst for water splitting application. The resultant Ru_{SA}-N-S-Ti₃C₂T_x catalyst coupled with n^+np^+ -Si photocathode enables photoelectrochemical H₂ production with exceptionally high photocurrent density of 37.6 mA/cm² under AM 1.5G illumination.